The Astrophysical Journal, 911:66 (12pp), 2021 April 10 https://doi.org/10.3847/1538-4357/abe85f

A First Chandra View of the Cool Core Cluster A1668: Offset Cooling and AGN Feedback Cycle

T. Pasini[1], M. Gitti[2,3], F. Brighenti[2], E. O'Sullivan[4], F. Gastaldello[5], P. Temi[6], and S. L. Hamer[7]
[1] Hamburger Sternwarte, Universität Hamburg, Gojenbergsweg 112, D-21029 Hamburg, Germany; thomas.pasini@hs.uni-hamburg.de
[2] Dipartimento di Fisica e Astronomia (DIFA), Universita' di Bologna, via Gobetti 93/2, I-40129 Bologna, Italy
[3] Istituto Nazionale di Astrofisica (INAF) - Istituto di Radioastronomia (IRA), via Gobetti 101, I-40129 Bologna, Italy
[4] Harvard-Smithsonian Center for Astrophysics, 60 Garden Street, Cambridge, MA02138, USA
[5] INAF-IASF Milano, via E. Bassini 15, I-20133 Milano, Italy
[6] Astrophysics Branch, NASA/Ames Research Center, MS 245-6, Moffett Field, CA 94035, USA
[7] Department of Physics, University of Bath, Claverton Down, BA2 7AY, UK
Received 2020 October 7; revised 2021 February 18; accepted 2021 February 18; published 2021 April 16

Abstract

We present a multiwavelength analysis of the cluster A1668, performed by means of new EVLA and Chandra observations and archival Hα data. The radio images exhibit a small central source ($\sim$14 kpc at 1.4 GHz) with $L_{1.4\text{GHz}} \sim 6 \cdot 10^{23}$ W Hz^{-1}. The mean spectral index between 1.4 GHz and 5 GHz is ~ -1, consistent with the usual indices found in BCGs. The cooling region extends for 40 kpc, with bolometric X-ray luminosity $L_{\text{cool}} = 1.9 \pm 0.1 \cdot 10^{43}$ erg s^{-1}. We detect an offset of $\sim$6 kpc between the cluster BCG and the X-ray peak, and another offset of $\sim$7.6 kpc between the Hα and the X-ray peaks. We discuss possible causes for these offsets, which suggest that the coolest gas is not condensing directly from the lowest-entropy gas. In particular, we argue that the cool ICM was drawn out from the core by sloshing, whereas the Hα filaments were pushed aside from the expanding radio galaxy lobes. We detect two putative X-ray cavities, spatially associated with the west radio lobe (cavity A) and the east radio lobe (cavity B). The cavity power and age of the system are $P_{\text{cav}} \sim 9 \times 10^{42}$ erg s^{-1} and $t_{\text{age}} \sim 5.2$ Myr, respectively. Evaluating the position of A1668 in the cooling luminosity–cavity power parameter space, we find that the AGN energy injection is currently consistent within the scatter of the relationship, suggesting that offset cooling is likely not breaking the AGN feedback cycle.

Unified Astronomy Thesaurus concepts: Galaxy clusters (584); Abell clusters (9); Active galactic nuclei (16); Radio lobes (1348); Radio sources (1358); Cooling flows (2028); Intracluster medium (858)

1. Introduction

In the last two decades, our understanding of the evolution of cool core galaxy clusters has led to a picture in which the cooling of the intracluster medium (ICM), the cold gas accreting onto the brightest cluster galaxy (BCG), and the feedback from the central radio source give birth to a tightly connected cycle, known as the active galactic nuclei (AGN) feedback loop; for reviews, see, e.g., McNamara & Nulsen (2007), Gitti et al. (2012), McNamara & Nulsen (2012), Fabian (2012), and Soker (2016). Multiwavelength data provide strong evidence of this cycle: cavities in the ICM, revealed through deep X-ray observations and induced by the jets of the central radio galaxy (e.g., McNamara et al. 2000; Bîrzan et al. 2004; Clarke et al. 2004; Fabian et al. 2006; Gentile et al. 2007); cold fronts (e.g., Fabian et al. 2006; Markevitch & Vikhlinin 2007; Gastaldello et al. 2009; Ghizzardi et al. 2010); optical line emission (Crawford et al. 1999; McDonald et al. 2010; Hamer et al. 2016); and dust filaments (Van Dokkum & Franx 1995; Laine et al. 2003) indicate an extremely complex and dynamical environment, the physical processes of which are still yet to be completely understood.

Recently, multiple studies have revealed strong links between the central BCG, the X-ray core, and the cluster dynamics (Sanderson et al. 2009; Hudson et al. 2010; Rossetti et al. 2016). In particular, spatial offsets between the BCG, the Hα line emission, and the X-ray emission peak (e.g., Haarsma et al. 2010; Hamer et al. 2012, 2016; Barbosa et al. 2018) suggest that ICM sloshing and offset cooling, together with the AGN, can have a significant influence on the cluster evolution. Indeed, all these elements affect the activity of the central supermassive black hole (SMBH) through motions of the gas that could be able to regulate the cavity production—and consequently, the feedback cycle as well, since the ICM oscillates back and forth with respect to the central SMBH.

This was recently discussed in Pasini et al. (2019) with regard to the cool core cluster A2495. Spatial offsets have been observed in this cluster, with the X-ray peak being separated by $\sim$6 kpc from the BCG and $\sim$4 kpc from the Hα line emission peak. The analysis presented by the authors on two putative systems of X-ray cavities, hinted at in the shallow ($\sim$8 ks) Chandra observation, suggests that even if cooling is not depositing gas onto the BCG core, the coupling between the AGN power output and the cooling rate is still consistent with the observed distribution for cluster samples. In a forthcoming publication, we will present a detailed analysis of the deeper Chandra observations of A2495, recently allocated ($\sim$130 ks, P.I. Gitti[8]), which will be key to probing the presence of the two pairs of ICM cavities and testing the proposed scenario that the feeding–feedback cycle is not broken.

A1668 was selected, along with A2495, from the ROSAT Brightest Cluster Sample (BCS; Ebeling et al. 1998) by choosing objects with X-ray fluxes greater than 10^{-11} erg cm^{-2} s^{-1}, and among these, by selecting those characterized by $\log L_{\text{H}\alpha} > 40$ from the catalog of Crawford et al. (1999). Of the obtained sample of 13 objects, A2495 and A1668 still lacked Chandra observations, which were obtained jointly with new VLA data

---

[8] Proposal Number 22800391.

Table 1
Radio Observations Properties (Project Code SC0143, P.I. M. Gitti)

Frequency	Number of Spectral Window	Channels	Bandwidth	Array	Total Exposure Time
5 GHz (C BAND)	2 (4832 MHz–4960 MHz)	64	128 MHz	B	$3^h59^m21^s$
1.4 GHz (L BAND)	2 (1264 MHz–1392 MHz)	64	128 MHz	A	$2^h59^m28^s$

(P.I. Gitti[9]). Pasini et al. (2019) have presented the results for A2495, also making use of Hα line emission data and Hubble Space Telescope (HST) archival images. In this work, we combine the A1668 VLA and Chandra new observations in order to study the interactions between the radio source hosted in the BCG and the ICM. In addition, for A2495, we also included Hα line emission data from Hamer et al. (2016); on the other hand, no HST data were available for this cluster.

A1668 was previously observed in the radio band by TGSS (TIFR GMRT Sky Survey), which gives an estimate for the 150 MHz flux density of 1589 ± 159 mJy; Hogan et al. (2015) performed a 5 GHz radio analysis (the data they used are not the same as the data presented in this work), estimating a flux density of 21.0 ± 0.1 mJy. A1668 was recently included by Bîrzan et al. (2020) in their sample of systems observed at 150 MHz by the LOw Frequency ARray (LOFAR; van Haarlem et al. 2013), showing the presence of large radio lobes, each extending for more than 50 kpc, and estimating a total flux density of 1.83 ± 0.44 Jy, consistent with TGSS.

Richness-based estimates of the mass provided values of $M_{200} \simeq 1.66 \cdot 10^{14}\, M_{\odot}$ (Andreon 2016) and $M_{2500} = 3.9\ \pm^{0.8}_{0.7} \cdot 10^{13}\, M\odot$ (Pulido et al. 2018). The cluster's BCG, IC4130, shows a star formation rate (SFR), estimated from extinction-corrected Hα luminosity obtained from long-slit observations, of $\mathrm{SFR} = 2.5 \pm 0.3\ M_{\odot}\ \mathrm{yr}^{-1}$ (Pulido et al. 2018), and extends for ∼85 kpc (diameter at the isophotal level of 25 mag arcsec^{-2} in the B-band; see Makarov et al. 2014).[10] Edwards et al. (2009) also presented IFU observations of the Hα emission close to the BCG, finding a clear velocity gradient from positive values north of the center to negative values at the south. They also argued that the line-emitting gas is likely not at rest with respect to the BCG.

In this work, we adopt a ΛCDM cosmology with $\mathrm{H}_0 = 73\ \mathrm{km\ s}^{-1}\ \mathrm{Mpc}^{-1}$, $\Omega_M = 1 - \Omega_\Lambda = 0.3$. The BCG redshift is $z = 0.06355$ (Hamer et al. 2016) and the luminosity distance is 273.7 Mpc, leading to a conversion of 1 arcsec = 1.173 kpc.

2. Radio Analysis

2.1. Observations and Data Reduction

IC4130, the BCG of A1668, was observed with the EVLA on 2011 June 17 in the 1.4 GHz band, and on 2011 March 9 in the 5 GHz band, in the A and B configurations, respectively. Details of the observations are shown in Table 1).

The sources J1331+3030 (3C286) and J1327+2210 were used for both the observations as flux and phase calibrators, respectively. The data reduction was performed using the NRAO Common Astronomy Software Applications package (CASA, version 5.3), applying the standard calibration procedure after carrying out an accurate editing of the visibilities with the CASA task `FLAGDATA`. We removed about 6% of the target visibilities at 5 GHz, whereas the data were highly contaminated by radio frequency interference (RFI) at 1.4GHz, thus producing a visibility loss of ∼40%.

We applied the standard imaging procedure, making use of the `CLEAN` task on a $7'' \times 7''$ region centered on the radio source. We accounted for the sky curvature by setting the `gridmode=WIDEFIELD` parameter and used a two-term approximation of the spectral model, exploiting the MS-MFFS algorithm (Rau & Cornwell 2011).

2.2. Results

We produced total intensity maps setting `weighting=BRIGGS`, corresponding to `ROBUST 0`. This baseline weighting provides the best compromise between angular resolution (determined by long baselines) and sensitivity to extended emission (provided by short baselines). The uncertainty on the flux density measurements is 5%, estimated from the amplitude calibration errors.

At 5 GHz (Figure 1), the radio source exhibits a total flux density of 19.9 ± 1.0 mJy, consistent with Hogan et al. (2015), that corresponds to a luminosity of $L_{5\,\mathrm{GHz}} = (1.8 \pm 0.1) \cdot 10^{23}\ \mathrm{W\ Hz}^{-1}$. The rms noise is 6 μJy beam^{-1}. The source stretches eastward for ∼11 kpc, with a minor axis of ∼5.7 kpc. There are no visible hints of larger emission up to the scale we are sensitive to (60 kpc with the VLA B configuration at 5 GHz). The equipartition field was estimated following the method described in Feretti & Giovannini (2008), finding $H_{\mathrm{eq}}(5\ \mathrm{GHz}) = 8.7 \pm 0.1\ \mu$G.

The 1.4 GHz map (`ROBUST 0`, Figure 2) shows no significant differences with respect to the 5 GHz emission. The source flux density is 70.2 ± 3.5 mJy and the rms is ∼17 μJy beam^{-1}. The radio source scale is slightly larger (∼14 kpc for the major axis, ∼7 kpc for the minor axis), with a more developed west lobe; again, we did not detect any hint of larger-scale emission up to our sensitivity scale (70 kpc with VLA A configuration at 1.4 GHz). Some cool core clusters show diffuse emission in the form of radio mini-halos (e.g., Gitti et al. 2004; Govoni et al. 2009; Giacintucci et al. 2014). Giacintucci et al. (2017) define a minimum radius of 50 kpc for mini-halos since, at smaller radii, diffusion and other transport mechanisms are plausibly able to spread the relativistic electrons from the central AGN within their synchrotron radiative cooling time. In Figures 1 and 2, the radio emission is coincident with the optical BCG, and the small scale suggests that it can all be attributed to the AGN/radio galaxy. It is possible that diffuse emission larger than our sensitivity scale exists; however, given the extended double-lobe morphology of the LOFAR 150 MHz image presented in Bîrzan et al. (2020), the presence of a mini-halo in A1668 seems unlikely. The equipartition field is $H_{\mathrm{eq}}(1.4\ \mathrm{GHz}) = 10.3 \pm 0.1\ \mu$G. Radio properties can be found in Table 2.

The radio source hosted in the center of A1668 can be classified as an FRI galaxy, as demonstrated by both the morphology (asymmetric lobes, no hotspots) and the 1.4 GHz luminosity ($L_{1.4\,\mathrm{GHz}} = (6.3 \pm 0.3) \cdot 10^{23}\ \mathrm{W\ Hz}^{-1}$), which place

---

[9] Proposal Number 12800143.

[10] HyperLEDA catalog.

Table 2
Radio Properties of A1668 in the Two Bands Observed

Band	Flux Density [mJy]	rms [μJy beam^{-1}]	Beam [arcsec]	Luminosity [10^{22} W Hz^{-1}]	Volume [kpc^3]	Brightness Temperature [K]	Equipartition Field [μG]
5 GHz	19.9 ± 1.0	6	1.14x1.00	16.8 ± 0.8	185 ± 22	39.6 ± 10.4	8.7 ± 0.1
1.4 GHz	70.2 ± 3.5	17	1.44x1.08	59.1 ± 2.9	359 ± 30	1129.3 ± 241.2	10.3 ± 0.1

Note. The axes of the radio galaxy are $a = 10.9 \pm 1.3$ kpc, $b = 5.7 \pm 1.3$ kpc for the 5 GHz map and $a = 14.0 \pm 1.3$ kpc, $b = 7.1 \pm 1.3$ kpc for the 1.4 GHz map. Flux is estimated within 3σ contours, while for the volume we assumed a prolate ellipsoid shape.

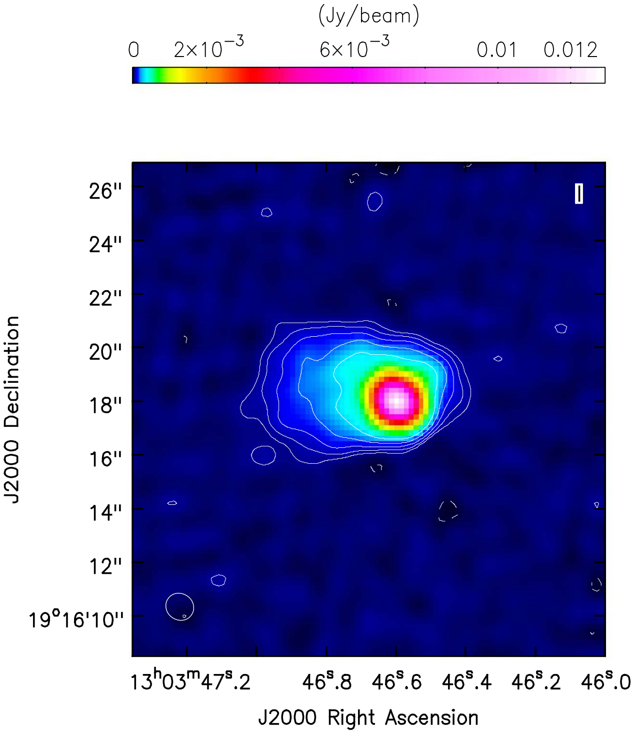

Figure 1. The 5 GHz VLA map (`ROBUST 0`) of the radio source hosted in IC4130, the BCG of A1668. Resolution is $1''.14 \times 1''.00$, with an rms noise of 6 μJy beam^{-1}. Contours are at $-3,3,6,12,24,48 \cdot$ rms. Source flux density is 19.9 ± 1.0 mJy. White ellipse at the bottom left represents the beam.

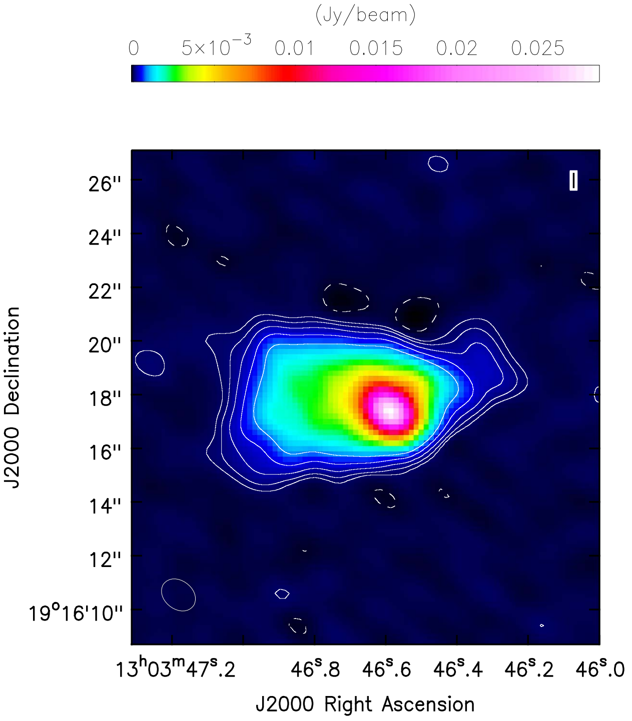

Figure 2. The 1.4 GHz VLA map (`ROBUST 0`) of the radio source hosted in IC4130. Resolution is $1''.44 \times 1''.08$, with an rms noise of 17 μJy beam^{-1}. Contours are at -3, 3, 6, 12, 24, $48 \cdot$ rms. Source flux density is 70.2 ± 3.5 mJy. White ellipse in the bottom left represents the beam.

IC4130 in the 70th percentile of the BCG radio luminosity function presented in Hogan et al. (2015).

2.2.1. Spectral Index Map

The synchrotron spectrum follows a power law $S_\nu \propto \nu^\alpha$, where α is the spectral index. The spectral index map (Figure 3) was generated using the CASA task `IMMATH`, combining 1.4 GHz and 5 GHz maps produced with matched `weighting=UNIFORM` (to enhance the resolution), `UVRANGE = 6.5-152`, and a resolution of $1''.4 \times 1''.0$. The `UVRANGE` was set in order to be sensitive to the same baselines (and thus, physical scales) for both observations.

Table 3 lists the peak, the extended, and the total radio emission flux densities at 5 and 1.4 GHz, together with the estimated spectral index between the two frequencies. The radio core exhibits a flat index ($\alpha \simeq 0$), as expected from optical thick regions where the radiation is self-absorbed. Moving toward the outskirt, the spectrum becomes steeper, reaching $\alpha \simeq -2.5$ in the outermost part. The mean index is -0.99 ± 0.06, consistent with the typical values found in BCGs (Hogan et al. 2015). Table 3 summarizes the spectral index properties.

3. X-Ray Analysis

3.1. Observation and Data Reduction

A1668 was observed with the Chandra Advanced CCD Imaging Spectrometer (ACIS), with the focal point on the S3 CCD, in cycle 12 (ObsID 12877, P.I. Gitti) for a total exposure of ∼10 ks. Data were reprocessed with CIAO 4.9 (Fruscione et al. 2006) using CALDB 4.2.1. We run the Chandra`_repro` script to perform the standard calibration process. After background flare removal, we used the `Blanksky` template files, filtered and normalized to the count rate of the source in the hard X-ray band (9–12 keV), in order to subtract the background. The final exposure time is 9979 s, with roughly ∼6800 net counts in a 100″ (∼120 kpc radius region (0.5–2 keV) centered on the cluster.

Point sources were identified and removed using the CIAO task `WAVDETECT`. Making use of optical catalogs, we found

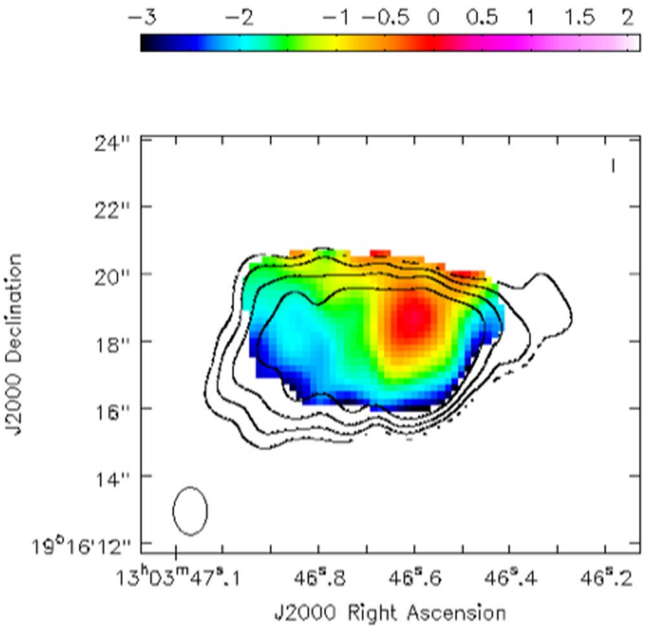

Figure 3. Spectral index map between 5 GHz and 1.4 GHz of the radio source hosted in IC4130. Contours are the same as Figure 2, and typical errors range from $\Delta\alpha \simeq 0.1$ for the inner and $\Delta\alpha \simeq 0.5$ for the outer regions.

Table 3
Flux Density Values at 5 GHz (C Band) and 1.4 GHz (L band)

Region	$S_C \pm \Delta S_C$ [mJy]	$S_L \pm \Delta S_L$ [mJy]	$\alpha \pm \Delta\alpha$
Peak	7.5 ± 0.4	17.6 ± 0.9	-0.67 ± 0.06
Extended	12.4 ± 0.6	52.6 ± 2.6	-1.13 ± 0.05
Total	19.9 ± 1.0	70.2 ± 3.5	-0.99 ± 0.06

Note. The first column shows values for the 5 GHz band, while the second column shows those for 1.4 GHz. The third column presents the corresponding spectral index values. The extended flux was estimated as the difference between the total and the peak flux densities.

that no astrometry correction was necessary. Unless otherwise stated, the reported errors are at 68% confidence level (1σ).

3.2. Results

3.2.1. Surface Brightness Profile

In Figure 4, we show the smoothed 0.5–2 keV image of A1668.

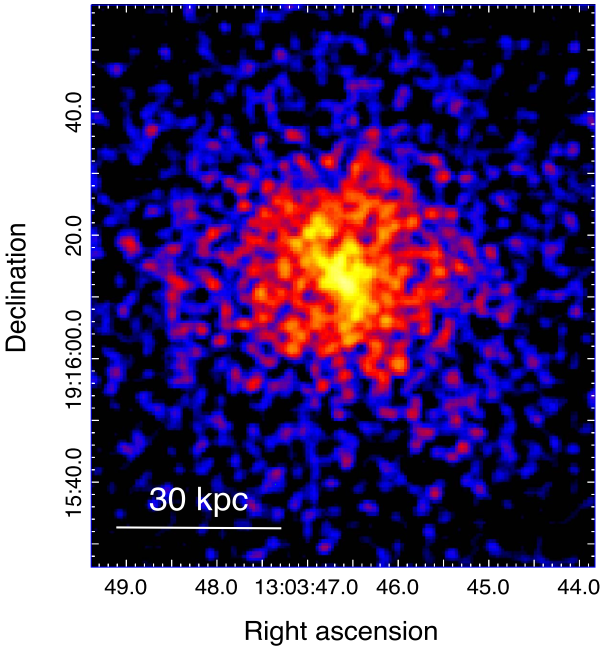

Figure 4. Chandra image of A1668 in the 0.5–2 keV band, smoothed with a Gaussian filter with a 3 pixel radius.

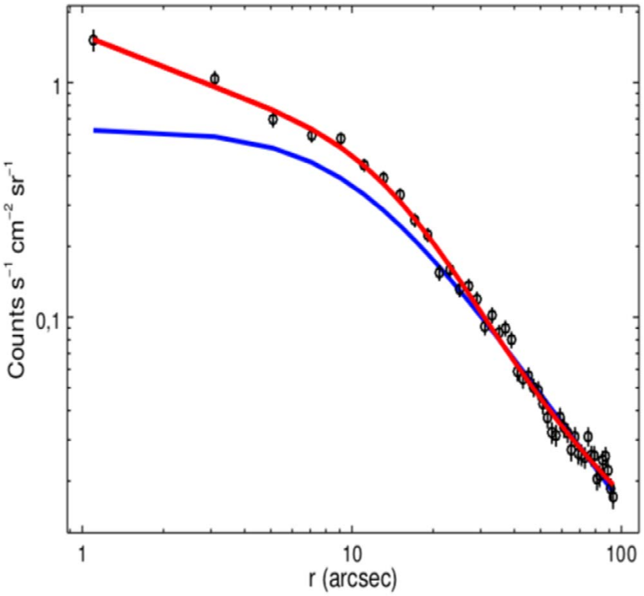

Figure 5. The 0.5–2 keV radial surface brightness profile of A1668. Blue line represents the single β-model fit performed in the external 30″–100″ interval and extrapolated to the center. Red line is the double β-model fit performed on every radius.

The ICM exhibits a roughly circular and regular morphology on large scales (>30″ 35 kpc), while the cluster core shows a region with enhanced emission in the NE-SW direction. Using the tool `SHERPA` (Freeman et al. 2001), a surface brightness profile was produced from a background-subtracted, exposure-corrected image, making use of 2″ wide concentric annuli centered on the X-ray peak. The profile was then fitted with a single β-Model (Cavaliere & Fusco-Femiano 1976) over the external 30″–100″ (35-120 kpc) interval, in order to exclude the whole core region.[11] The result of the fit (χ^2/DoF ∼1.71) and its extrapolation to the core region is represented with the blue line in Figure 5. The best-fit values are: core radius `r0` $= 10.0 \pm^{0.7}_{0.4}$ arcsec (∼11.8 kpc), `beta` $= 0.43 \pm^{0.04}_{0.02}$, and central surface brightness `ampl` $= 0.64 \pm^{0.10}_{0.04}$ counts s^{-1} cm^{-2} sr^{-1}.

The central brightness excess with respect to the β-model is a strong indication of the presence of a cool core in A1668, as we expected from the selection criteria described in Section 1. This will also be confirmed by the spectral analysis (see Section 3.2.2). We therefore fitted the same profile on the entire radial range with a double β-model (Mohr et al. 1999; LaRoque et al. 2006), represented by the red line in Figure 5 (χ^2/DoF ∼1.49), which provides a better description of the real trend: we found `r0`$_1 = 15.6 \pm^{4.2}_{2.7}$ arcsec (∼18.3 kpc),

---

[11] The assumption of 30″, which was already justifiable through visual inspection, will be further supported by the estimate of the cooling radius in Section 3.2.2.

Table 4
Fit Results for the Projected Analysis

$r_{\min} - r_{\max}$ [arcsec]	$r_{\min} - r_{\max}$ [kpc]	Counts	$\mathrm{kT} \pm \sigma_{\mathrm{kT}}$ [keV]	χ^2/ DoF
0–12	0–14	1346 (99.6%)	$1.74 \pm^{0.15}_{0.08}$	45/42
12–21	14–25	1274 (99.1%)	$2.09 \pm^{0.33}_{0.16}$	62/47
21–33	25–35	1328 (97.8%)	$2.84 \pm^{0.39}_{0.36}$	68/52
33–45	35–53	1111 (96.9%)	$3.65 \pm^{0.66}_{0.51}$	60/50
45–60	53–70	1101 (93.8%)	$4.05 \pm^{0.90}_{0.66}$	78/58
60–75	70–88	947 (91.2%)	$3.39 \pm^{0.81}_{0.54}$	123/61
75–90	88–106	1006 (89.2%)	$3.51 \pm^{0.75}_{0.55}$	98/64

Note. The first and second columns show the lower and upper limits of the extraction rings in arcsec and kpc, while the third column represents the number of source photons coming from each ring, with the percentage indicating their number compared to the total photons of the same region. In the last two columns, we report the values of kT, with associated errors, as well as the χ^2/ DoF.

`beta`$_1 = 0.67 \pm^{0.14}_{0.08}$, and `ampl`$_1 = 0.59 \pm^{0.11}_{0.14}$ counts s^{-1} cm^{-2} sr^{-1} for the first β-model, and `r0`$_2 = 0.64 \pm^{0.32}_{0.76}$ arcsec, `beta`$_2 = 0.42 \pm^{0.02}_{0.01}$, and `ampl`$_2 = 1.78 \pm^{0.75}_{3.07}$ counts s^{-1} cm^{-2} sr^{-1} for the second β-model.

3.2.2. Spectral Analysis

Spectra were extracted with the CIAO task `specextract` in the 0.5–7 keV band; the extraction was made from a series of concentric rings centered on the X-ray peak. Each region contains at least ~1000 net counts. Background spectra were also extracted from the `Blanksky` files of each region. We individually fitted every spectrum via `Xspec` (Arnaud 1996, vv.12.9.1) using a `phabs*apec` model, approximating an absorbed, collisionally ionized, diffuse gas. The redshift was fixed at $z = 0.06355$ and the hydrogen column density was fixed at $N_H = 2.20 \cdot 10^{20}$ cm^{-2} (estimated from Kalberla et al. (2005)). The normalization parameter and the temperature kT were left free to vary. The observation was too shallow to allow us to fit metallicity, which was instead kept fixed at a value of 0.3 $Z_\odot$[12,13]. Note that these fits do not take projection effects into account. The best-fitting parameters are listed in Table 4. The projected temperature profile of A1668 is shown in blue in Figure 6.

Projection effects were then taken into account by extracting spectra from concentric rings centered on the X-ray peak, containing more than 1500 counts, and fitting them with a `projct*phabs*apec` model. Temperature and normalization were left free to vary, while column density, redshift, and abundance were frozen at the same values of the projected analysis above. Results are listed in Table 5. The deprojected temperature profile of the cluster is shown in black in Figure 6.

Following the same method described in Pasini et al. (2019)[14], we estimated the electronic density as:

$$n_e = \sqrt{10^{14}\left(\frac{4\pi \cdot N(r) \cdot [D_A \cdot (1+z)]^2}{0.82 \cdot V}\right)}, \tag{1}$$

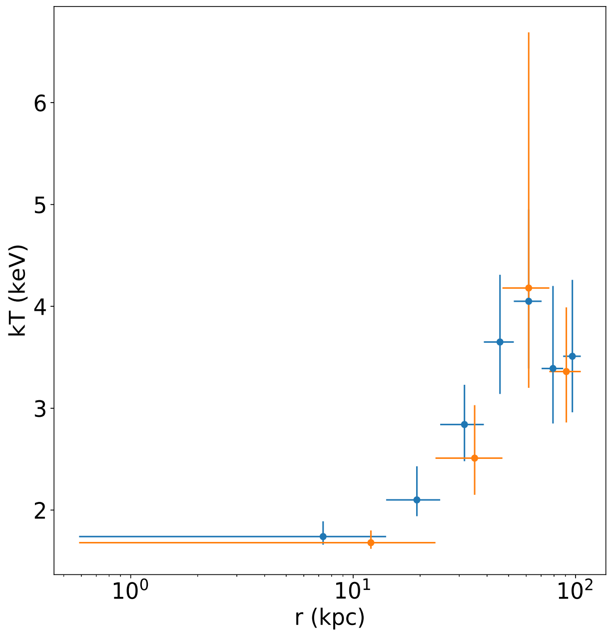

Figure 6. Projected (blue) and deprojected (yellow) temperature profile of A1668. Bars in the *x*-axis represent the range of the extraction rings, while those in the *y*-axis are the errors for the temperature values.

where $N(r)$ is the `apec` normalization of the deprojected model, V is the shell volume, and D_A is the angular distance of the source, estimated as $D_A = D_L/(1+z)^2$. Table 5 lists the density values for each ring, with the results showed in Figure 7.

Making use of the deprojected temperature and density values, we can derive the cooling time, the pressure, and the entropy for each bin. Table 5 presents the pressure values, calculated as $p = 1.83 n_e kT$, while the entropy, which was estimated as $S = kTn_e^{-2/3}$, is presented in Figure 8.

The cooling time is defined as:

$$t_{\mathrm{cool}} = \frac{H}{\Lambda(T) n_e n_p} = \frac{\gamma}{\gamma - 1}\frac{kT(r)}{\mu X n_e(r)\Lambda(T)}, \tag{2}$$

where $\gamma = 5/3$ is the adiabatic index, H is the enthalpy, $\mu \simeq 0.61$ is the molecular weight for a fully ionized plasma, $X \simeq 0.71$ is the hydrogen mass fraction, and $\Lambda(T)$ is the cooling function (Sutherland & Dopita 1993). Results are listed in Table 5, while the cooling time radial profile is shown in Figure 9.

We thus estimated the cooling radius of the cluster, i.e., the radius within which the ICM cooling is efficient, assuming $t_{\mathrm{age}} \sim 7.7$ Gyr, corresponding to the look-back time at $z = 1$, as an upper limit for the cluster age. Consequently, the intersection between the profile best fit (blue line) and t_{age} (red line) defines the cooling radius of A1668, being $r_{\mathrm{cool}} \approx 34'' \approx 40$ kpc.

The bolometric X-ray luminosity emitted within this radius was estimated by extracting a spectrum from an annular region centered on the X-ray peak with $r = r_{\mathrm{cool}}$. Projection effects were taken into account using a second annular region with internal radius coincident with r_{cool} and external radius ~100″. By fitting both spectra with a `projct*phabs*apec` model, the bolometric luminosity inside the cooling region yields a value of $L_{\mathrm{cool}} = 1.9 \pm 0.1 \cdot 10^{43}$ erg s^{-1}. Assuming a steady-state cooling flow model, the *mass deposition rate* of the

---

[12] This value was assumed after we tried to leave the metallicity free to vary. However, error bars were too large to keep it thawed.

[13] The exploited abundance table is from Anders & Grevesse (1989).

[14] Note the typo in Equation (4) of that paper.

Table 5
Fit Results for the Deprojected Analysis

$r_{\min}$–$r_{\max}$ [arcsec]	$r_{\min}$–$r_{\max}$ [kpc]	Counts	kT [keV]	$N(r)$ (10^{-4})	Electronic Density [10^{-2} cm^{-3}]	Pressure [10^{-11} dy cm^{-2}]	Entropy [keV cm^2]	$t_{\rm cool}$ [Gyr]
0–20	0–23.5	2506 (99.4%)	$1.68\ \pm^{0.12}_{0.06}$	$10.3\ \pm^{0.6}_{0.6}$	$2.67\ \pm^{0.01}_{0.01}$	$13.4\ \pm^{1.1}_{0.4}$	$19.5\ \pm^{0.5}_{0.2}$	$1.4\ \pm^{0.1}_{0.1}$
20–40	23.5–46.9	2162(97.4%)	$2.51\ \pm^{0.52}_{0.36}$	$12.5\ \pm^{0.8}_{0.8}$	$1.07\ \pm^{0.01}_{0.01}$	$7.7\ \pm^{1.4}_{1.0}$	$51.8\ \pm^{2.0}_{1.4}$	$4.3\ \pm^{0.6}_{0.6}$
40–65	46.9–76.2	1862 (93.7%)	$4.18\ \pm^{2.51}_{0.98}$	$8.1\ \pm^{0.8}_{0.8}$	$0.44\ \pm^{0.01}_{0.01}$	$7.5\ \pm^{5.1}_{2.4}$	$219.9\ \pm^{24.5}_{11.3}$	$15.8\ \pm^{5.2}_{5.1}$
65–90	76.2–105.5	1653 (89.1%)	$3.36\ \pm^{0.63}_{0.50}$	$16.9\ \pm^{0.9}_{0.9}$	$0.44\ \pm^{0.01}_{0.01}$	$4.2\ \pm^{0.7}_{0.6}$	$120.7\ \pm^{3.5}_{3.0}$	$11.7\ \pm^{1.7}_{1.8}$

Note. The first three columns report the limits of the annular regions and the number of source photons from each ring, with the percentage indicating their number compared to the total photons of the same region. The remaining columns report temperature, normalization factor, electronic density, pressure, entropy, and cooling time. The fit gives $\chi^2/$ DoF = 1.46.

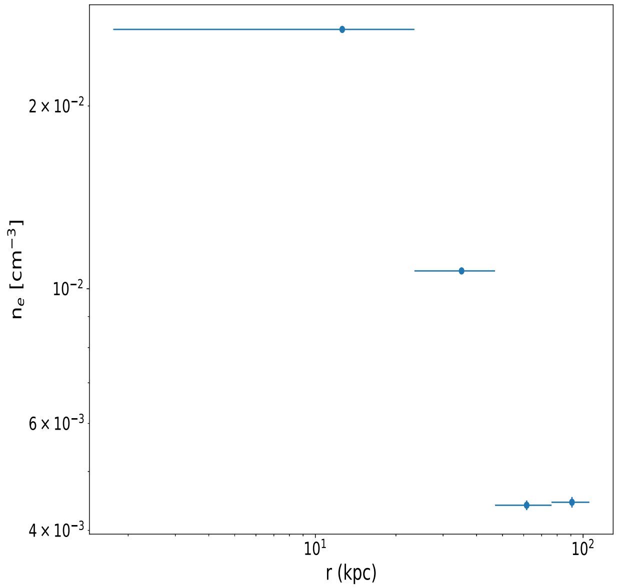

Figure 7. Density radial profile of A1668 derived from the deprojected analysis. Each bin defines an extraction region.

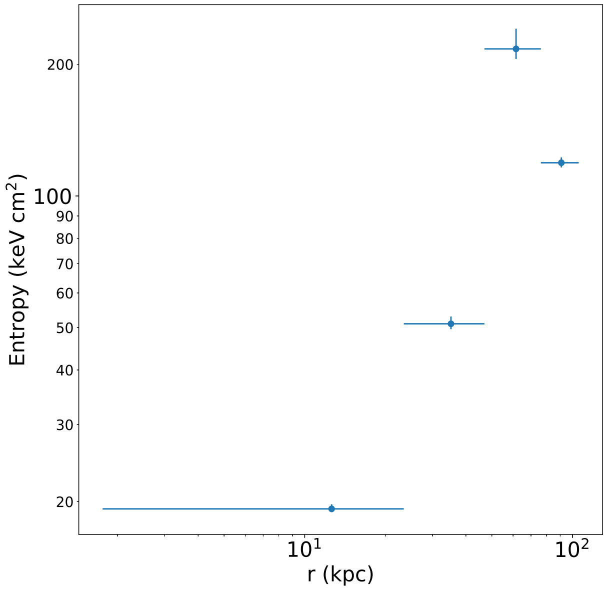

Figure 8. Entropy radial profile of A1668 derived from the deprojected analysis. Each bin defines an extraction region.

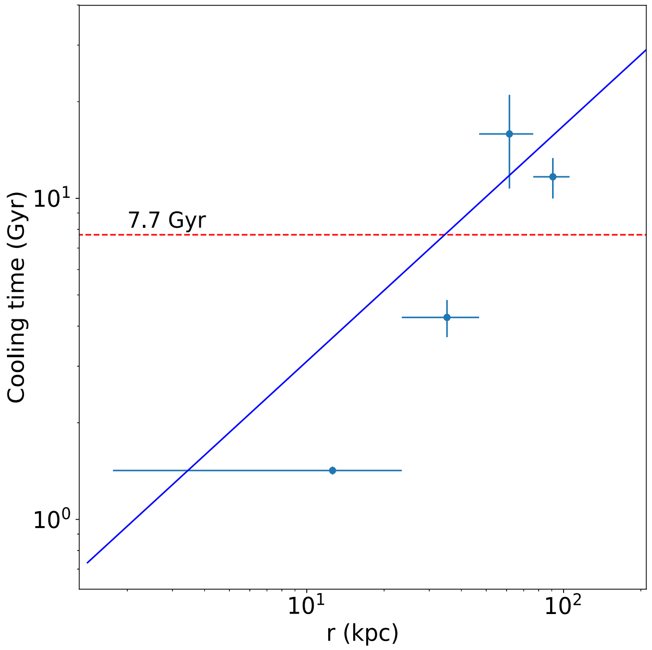

Figure 9. Cooling time profile of A1668. Each bin defines an extraction region. Blue line represents the best-fit function $f(x) = (0.57 \pm 0.99)x^{0.73\pm0.43}$, while red line is $t_{\rm age} = 7.7$ Gyr.

cooling flow of A1668 can be estimated as:

$$\dot{M} \simeq \frac{2}{5}\frac{\mu m_p}{kT} \cdot L_{\rm cool}. \tag{3}$$

In this way, we obtain $\dot{M} \simeq 29.6 \pm 1.6\ M_\odot$ yr^{-1}.

As a different approach, we performed a further fit of the spectrum of the cooling region with a `phabs *(apec + mkcflow)` model, where the `apec` component approximates the ICM emission along the line of sight outside the cooling region, while `mkcflow` is a multiphase component reproducing a cooling-flow-like emission inside the cooling radius. As above, the abundance was fixed at 0.3 $Z_\odot$, while the temperature of the `apec` model was left free to vary and bounded to the `high temperature` parameter of `mkcflow`. Redshift and absorbing column density were fixed at the Galactic values (see above), while the `low temperature` parameter of `mkcflow` was fixed at the lowest possible value, ~0.1 keV. The fit gives χ^2/DoF = 105/100 and provides an upper limit of $\dot{M} < 5\ M_\odot$ yr^{-1}. The bolometric luminosity associated to the `mkcflow` model is $L_{\rm mkcflow} = 3.2 \pm$

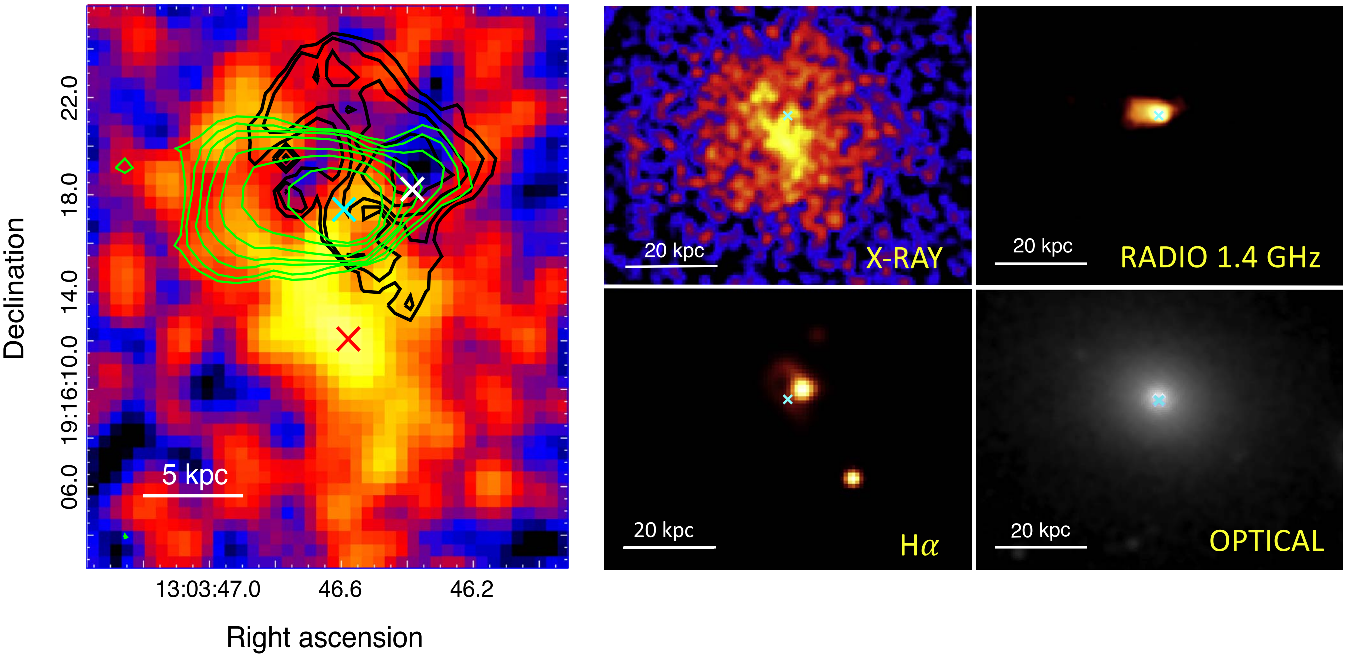

Figure 10. Left panel shows 1.4 GHz radio (green) and Hα (black) contours overlaid on the 0.5–2 keV X-ray image, zoomed toward the cluster center. Cyan cross represents the X-ray emission centroid, coincident with the BCG center; red and white crosses are the X-ray and Hα peaks, respectively. In the right panel, going from left to right and top to bottom, are shown 0.5–2 keV, 1.4 GHz, Hα, and optical (SDSS) images of A1668, respectively. All images are centered on the X-ray peak. Cyan cross represents the BCG.

$0.1 \cdot 10^{41}$ erg s^{-1}. The difference between the two estimates of the mass deposition rate reflects the *cooling flow (CF) problem*: observed mass deposition rates do not match expectations from the standard CF model, and heating contribution, likely produced by the central AGN, is required to balance the ICM radiative losses.

4. Discussion

4.1. Radio–X-Ray Combined Analysis

In order to investigate the interactions between the cooling ICM and the BCG, we overlaid the 1.4 GHz radio contours onto the X-ray 0.5–2 keV cluster image. Since we are interested in the core region, in Figure 10 we show the resulting image, zoomed in the central 30 × 30 kpc.

The cluster X-ray cool core exhibits an elliptical nuclear region. Exploiting optical catalogs, we found that the radio galaxy is coincident with the BCG nuclear region, as expected. The emission centroid of the large-scale X-ray emission (R.A. $= 13^{\rm h}03^{\rm m}43\overset{\rm s}{.}6$, decl. $= +19°16^{\rm m}17\overset{\rm s}{.}4$), defined as the center of the isophotes, also lies within this region. On the other hand, the X-ray peak (R.A. $= 13^{\rm h}03^{\rm m}46\overset{\rm s}{.}6$, decl. $= +19°16^{\rm m}12.2^{\rm s}$), is found to the south of the nucleus of the BCG, exhibiting a significant offset of $\sim 5\overset{\prime\prime}{.}2$, corresponding to ∼6 kpc.

In order to check on the possible presence of a field point source that could bias the detection of the X-ray peak, we extracted a spectrum from a $\sim 4''$ circular region centered on the peak, and fitted it with two models: `phabs*apec` and `phabs*(apec+powerlaw)`. The first fit gave $\chi^2/\mathrm{DoF} \sim 78/79$, while for the second, $\chi^2/\mathrm{DoF} \sim 71/77$; the F-stat method was then applied in order to check whether the addition of the `powerlaw` component provided a significant improvement of the fit. We obtained an F-value of 3.4 and $p = 0.035$, corresponding to a null hypothesis probability of 1-$p = 0.965$. This suggests that the addition of the point-source emission component is not statistically significant. As a further check, we looked for possible point-sources in high-energy, optical, and infrared catalogs, as well as in a harder-band (4–7 keV) X-ray image; however, we did not detect any point source coincident with the X-ray peak. We thus conclude that the peak detection is likely not biased, and therefore the offset is real.

This is analogous with what was found in A2495, which presents a offset of similar scale between these two components, and with a number of recent works that found the same feature in other clusters, e.g., Sanderson et al. (2009) Haarsma et al. (2010), Hudson et al. (2010), Rossetti et al. (2016), and others; for a brief review of the state-of-the-art literature about BCG/cool core offsets, see Pasini et al. (2019). We will revisit this topic in Section 4.3.

A two-dimensional temperature map is often used in order to further investigate the cluster structure and its thermodynamic state, but the small number of photons prevents us from producing such map. We also estimated the *softness ratio* as (S-H)/(S+H), where S and H are the number of counts in the soft (0.5–2 keV) and hard (2–7 keV) bands, respectively. However, the statistics are still too poor and the errors too large to draw any conclusion from such analysis.

4.2. Hα Analysis

The presence of optical-line-emitting nebulae in galaxy clusters is linked to the thermodynamic conditions of the cluster core; observational studies (e.g., Cavagnolo et al. 2008; McNamara et al. 2016) have argued that such warm structures are only found if the central (∼10 kpc) entropy falls below 30 keV cm^2, or alternatively, when $t_{\rm cool}/t_{ff} < 10$–20 (Voit et al. 2015), where $t_{ff} = \sqrt{2R^3/GM}$ is the *freefall* time. The estimated

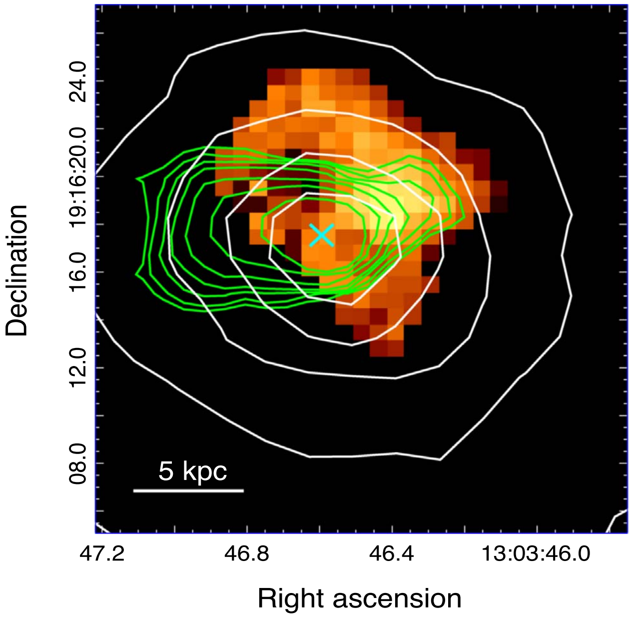

Figure 11. The 1.4 GHz radio (green) contours overlaid on the VIMOS Hα image (Hamer et al. 2016). Mean seeing is 1″.21, and map units are in 10^{-16} erg s^{-1} cm^{-2} Å. White contours are the optical isophotes from SDSS. Cyan cross represents the radio galaxy center, coincident with the BCG core.

entropy within the central bin of our spectral analysis ($r < 23.5$ kpc, Table 5) is ~19.5 keV cm^2, thus satisfying the criterion for the presence of such nebulae in A1668. Hamer et al. (2016) presented VIMOS observations of the Hα line emission of a sample of 73 BCGs, including A1668, whose image is shown in Figure 11.

The Hα structure presents a rather compact shape, extending for ~9″ (~10.6 kpc). Its total luminosity is $L_{\mathrm{H}\alpha} = 3.85 \pm 0.30 \cdot 10^{40}$ erg s^{-1}[15], and Hamer et al. (2016) classified it as a quiescent object, showing a simple, centrally concentrated morphology.[16] To better visualize the interplay of the three components, in Figure 10 we also overlay the Hα contours onto the X-ray 0.5–2 keV image.

The line emission lies entirely within the BCG, but although it is also within the cool core as defined from the cooling time profile, it only overlaps one end of the bright X-ray ridge. This highlights a difference from A2495, in which the Hα structure connects the galaxy with the X-ray peak, and from other systems (e.g., Bayer-Kim et al. 2002; Hamer et al. 2012, 2016), in which the line emission seems to be mostly associated with the cooling ICM rather than the BCG.

A significant offset of ~6.5″ (~7.6 kpc) is present between the Hα (R.A. = $13^{\mathrm{h}}03^{\mathrm{m}}46^{\mathrm{s}}.4$, decl. = $+19°16^{\mathrm{m}}18.1^{\mathrm{s}}$) and the X-ray peaks. The same feature, albeit smaller, was found in A2495 by Pasini et al. (2019); offsets between these two peaks were also detected in A1795 (Crawford et al. 2005) and in multiple systems by Hamer et al. (2016). We will revisit this topic in Section 4.3.

As Hamer et al. (2012) describe in greater detail, the ratio of the Hα plume extent and the total velocity gradient of the warm gas provides a estimate of the projected offset timescale. Pasini et al. (2019) showed that, for A2495, such a timescale is comparable to the age difference between two putative cavity pairs, suggesting that, for systems where the BCG oscillates back and forth through the cooling region, this measure could be a good indicator for the AGN cycle intermittency. In A1668, the Hα structure extends for $D' \sim 7''.7$ from the BCG center, corresponding to ~9 kpc, and showing a very smooth velocity gradient from east to west. We measured a velocity difference of ~+500 km s^{-1} between the gas at the BCG center and that at the tail of the Hα structure. This indicates a projected timescale of $T' = D'/V \sim 18$ Myr. In order to correct for the projection effects, we assumed a most likely inclination of ~60°, with a range of 30°–75° (Hamer et al. 2012); the corrected timescale can thus be estimated as $T = T' \times \cos[\mathrm{i}]/\mathrm{sen}[\mathrm{i}]$, with i being the inclination. In this way, we obtained an offset timescale of ~10.4 Myr, with an upper and a lower limit of ~31.2 and ~4.8 Myr, respectively; this is consistent with the value of ~13 Myr estimated for A2495, suggesting that the cold gas dynamics in the two systems are similar and that the timescale of AGN feedback intermittency is comparable.

One can also estimate the mass of the warm gas by assuming that it is optically thin:

$$M_{\mathrm{H}\alpha} \simeq L_{\mathrm{H}\alpha} \frac{4 \mu m_p}{n_{\mathrm{H}\alpha}\, \epsilon_{\mathrm{H}\alpha}}, \tag{4}$$

where $\epsilon_{\mathrm{H}\alpha} \sim 3.3 \cdot 10^{-25}$ erg cm^3 s^{-1} is the Hα line emissivity, while $n_{\mathrm{H}}\alpha$ is obtained assuming pressure equilibrium with the local ICM:

$$n_{\mathrm{H}\alpha} T_{\mathrm{H}\alpha} \simeq n_{\mathrm{ICM}} T_{\mathrm{ICM}}, \tag{5}$$

where $T_{\mathrm{H}}\alpha \sim 10^4$ K, T_{ICM} is the first value reported in Table 4 (~1.74 keV, since the Hα structure is located within the first spectral bin), and $n_{\mathrm{ICM}} \sim 1.83 n_e$, where n_e is the electronic density reported in the first row of Table 5. In this way, we obtain $M_{\mathrm{H}}\alpha \sim (2.4 \pm 0.2) \cdot 10^6 M_{\odot}$.

The [SII]$_\lambda$6716/[SII]$_\lambda$6731 line ratio provides an independent estimate of the density of the ionized gas and is measured in Appendix F of Hamer et al. (2016) as 1.21 ± 0.2. Assuming case B reionization and a temperature of 10^4 K, this gives an electron density of $n_{e,\mathrm{H}\alpha} = 350 \pm 270$ cm^{-3}, which corresponds to a total density of $n_{\mathrm{H}\alpha} = 640 \pm 495$ cm^{-3}. These values are comparable, within the (large) uncertainties, with the value of $n_{\mathrm{H}\alpha} = 100 \pm^{8}_{3}$ cm^{-3} derived from Equation (5). However, it is important to consider the impact of the assumed ionized gas temperature ($T_{\mathrm{H}\alpha}$) on the two measurements. A lower $T_{\mathrm{H}\alpha}$ would result in a higher $n_{e,\mathrm{H}\alpha}$ from Equation (5) but a lower $n_{e,\mathrm{H}\alpha}$ from the [SII]$_\lambda$6716/[SII]$_\lambda$6731 line ratio measurement, while a higher $T_{\mathrm{H}\alpha}$ would have the opposite effect on both measurements. The VIMOS data from Hamer et al. (2016) are not sensitive enough to provide a reliable estimate of $T_{\mathrm{H}\alpha}$ for Abell 1668, but deep observations of other objects have found upper limits to $T_{\mathrm{H}\alpha}$ that are much lower than expected (e.g., $T_{\mathrm{H}\alpha} < 5685$ K in the Centaurus cluster; see Hamer et al. 2019). Assuming $T_{\mathrm{H}\alpha} = 5000$ K, we find $n_e = 230 \pm 180$ cm^{-3} and $n_{\mathrm{H}\alpha} = 420 \pm 330$ cm^{-3} from the [SII] ratio and $n_{\mathrm{H}\alpha} = 200 \pm^{16}_{6}$ cm^{-3} derived from Equation (5), indicating that the two measurements are consistent within the limits of the available data and assumed values.

---

[15] This estimate differs from Pulido et al. (2018), as it is obtained from IFU observations and has not been extinction-corrected.

[16] The morphology looks slightly different when compared to Edwards et al. (2009), whose IFU image shows a shape that is somehow "resolved" better.

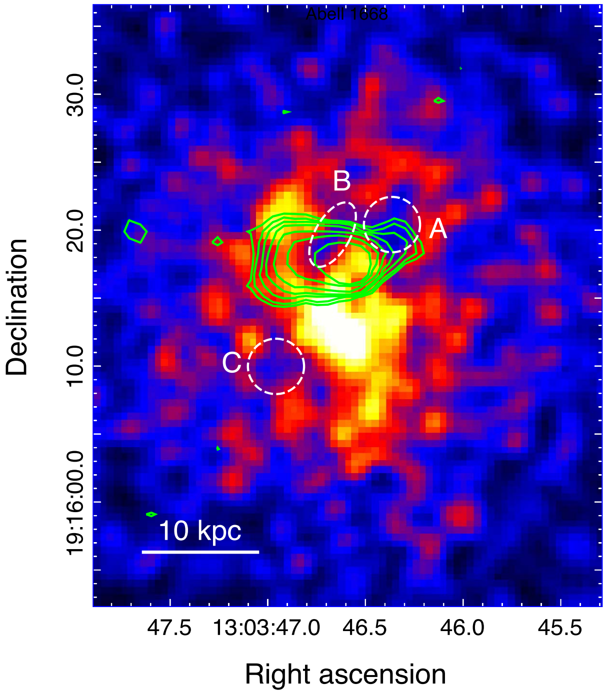

Figure 12. The 0.5–7 keV image showing three surface brightness depressions: A and B lie in the west and east lobes of the radio galaxy, respectively, while C is found at the opposite side of the core. Overlaid are the 1.4 GHz contours.

4.3. Putative Cavities and AGN Feedback Cycle

From the 0.5–2 keV X-ray image (see Figure 12), it is possible to identify a number of ICM surface brightness depressions. The present observation is very shallow (∼10 ks), and thus the reader should be warned about the significance of these deficits, which could possibly be artifacts. However, we have focused our attention on three of these features (shown in Figure 12) that, due to their position, could possibly represent real ICM cavities. One of them (A) lies within the west lobe of the radio galaxy; another surface brightness depression (B) is detected in the east lobe of the radio galaxy, while a symmetrical (with respect to the X-ray peak), similarly shaped brightness depression (C), is found at the opposite side of the cluster core, not associated with the radio galaxy. It is noteworthy that cavity A is also coincident with the Hα line emission peak.

To investigate these features, we estimated their significance as N_M-$\mathrm{N_C}/\sqrt{N_M + N_\mathrm{C}}$, where N_M and N_C are the number of counts in regions of equal area close to the candidate cavity and within the cavity, respectively. The number of counts varies depending on the size of the elliptical region chosen to cover the putative cavity, and as previously stated, the current observation requires us to be cautious because the shape and extent of the depression observed "by eye" can slightly change using different color scales. For this reason, the upper and lower limits for the dimensions of these regions were estimated by varying the axes of the ellipse until reaching a significance of 2σ and 3σ, respectively. The assumed "true" size of the bubble is the mean between these two limits. Cavity A exhibits a circular shape, with a diameter of 4.8 ± 0.6 kpc, while cavity B is more elliptical, with a major axis of 5.2 ± 0.4 kpc and a minor axis of 3.0 ± 0.3 kpc. On the other hand, the brightness deficit related to candidate cavity C is less enhanced, and in order to reach the desired significance, requires the size to be larger than the observed depression. Therefore, in the following analysis, we will only discuss candidate cavities A and B, while cavity C will not be considered. Following the method described in Bîrzan et al. (2004), we determined the cavity power:

$$P_\mathrm{cav} = \frac{E_\mathrm{cav}}{t_\mathrm{cav}} = \frac{4pV}{t_\mathrm{cav}}, \tag{6}$$

where t_cav is the age of the cavity, calculated as $t_\mathrm{cav} = R/c_s$, with R being the cavity distance from the BCG center, p is the pressure at the distance of the cavity, V is the cavity volume, and c_s is the sound velocity. The volume was estimated assuming an oblate ellipsoidal shape for both cavities, while for pressure and temperature we assumed the values listed in Table 5 corresponding to the annular bin the cavities lie in.

We obtained the same age for both cavities: $t_\mathrm{cav} = 5.2 \pm 0.7$ Myr. This leads to $P_\mathrm{cav,\ A} = 5.1 \pm 2.6 \cdot 10^{42}\ \mathrm{erg\ s^{-1}}$ for cavity A, and $P_\mathrm{cav,\ B} = 3.8 \pm 1.4 \cdot 10^{42}\ \mathrm{erg\ s^{-1}}$ for cavity B. This age is consistent with the offset timescale estimated in Section 4.2. Finally, we compared the estimated values of P_cav (based on the hypothesis that the cavities are real) and L_cool with the typical distribution observed for cool core clusters (Bîrzan et al. 2017). The results are presented in Figure 13.

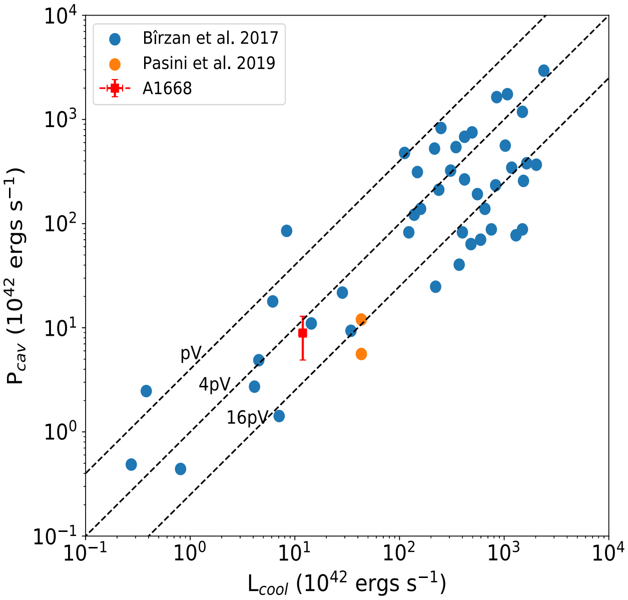

Figure 13. Blue points are the data from Bîrzan et al. (2017), orange ones are the values for A2495 (Pasini et al. 2019), while red represents the cavity system detected in A1668. Dashed lines represent, from left to right, $P_\mathrm{cav} = L_\mathrm{cool}$ assuming pV, $4pV$, or $16pV$ as the deposited energy.

The L_cool–P_cav relationship in A1668 is consistent within the scatter of the expected distribution, despite being on its lower edge. The detected offsets, therefore, do not seem to affect the feeding–feedback cycle, that is still maintained. The same result was found in A2495, where the two cavity systems (i.e., the AGN) have enough energy to balance the radiative losses within the cooling region. We then argue that small offsets are not able to break the AGN feeding–feedback cycle.

4.4. Offsets, Cooling, and Hα Emission: Are Sloshing and AGN Activity Shaping the Core of A1668?

As described in the previous sections, the core of A1668 contains a complex set of structures whose origins are not immediately clear. It is worth reiterating that the available Chandra data is only a snapshot, providing somewhat limited information on the ICM. It should also be remembered that all of the structures we observe are contained within the central ∼20 kpc, inside the stellar body of the BCG.

The offsets between the peaks of the radio, X-ray, and Hα emission raise the question of how these components came to be separated. The peak of emission from the hot ICM lies not in the BCG nucleus, but ∼6 kpc to the south. The radio emission is reasonably evenly distributed to the east and west of the nucleus, but the Hα peaks in the region of the west radio jet/lobe, extending around the western half of the radio structure and overlapping the optical centroid of the BCG.

We can suggest a qualitative scenario that might explain the relative morphologies of the different components. At some point in the past, A1668 may have been a relaxed cluster with a cool core. In that core, centered on the BCG, gas began to cool and condense out of the ICM, forming the kind of filamentary Hα nebula observed in other cool core cluster. The small velocity gradient in the Hα emission is consistent with such an origin. At that stage, A1668 underwent a minor merger, which caused the core to begin sloshing, oscillating around the center of the cluster gravitational potential. Sloshing motions in the plane of the sky are typically visible as a spiral pattern in the ICM, but if the plane of motion is aligned along the line of sight, the motions produce pairs of nested cold fronts, and the cool ICM gas drawn out from the core can appear as a tail to one side of the BCG. Our Chandra observation is too short for fronts to be visible, but we do see the tail: the ridge structure.

At this stage, cooling (and Hα emission) would still have been centered in the core of the BCG. About 5 Myr ago (∼cavity age), sufficient cooled material reached the central SMBH to trigger an outburst. This produced the radio jets/lobes we observe, and as these expanded, they pushed aside the pre-existing Hα filaments and hotter ICM gas. This produced a correlated Hα/radio morphology, with much of the Hα wrapped around the west jet/lobe. It also disrupted the center of the cool core, reducing the X-ray surface brightness as a large part of the volume in the core of the BCG was filled by the radio lobes, producing the apparent cavities in the ICM. This brings us to the current situation, where the brightest X-ray emission is in the tail to the south of the BCG nucleus.

The expansion timescale of the radio lobes is only a few 10^6 yr. This is very short compared to typical sloshing timescales. The hot ICM oscillates with the sloshing timescale given by $t_{\rm slosh} = 2\pi/\omega_{\rm BV}$, where $\omega_{\rm BV} = \Omega_K \left(\frac{1}{\gamma}\frac{d\ln S}{d\ln r}\right)^{1/2}$. Here, $d{\rm ls}S/d{\rm ln}r$ is the logarithmic entropy gradient, $\Omega_K = \sqrt{GM/r^3}$, and $\gamma = 5/3$ for the ionized ICM plasma. We also know that the freefall time in the cluster is $t_{\rm ff} = \sqrt{2r/g}$. Our Chandra data are not sufficient to accurately model the mass profile, but we know that the stellar velocity dispersion, σ_*, in the inner regions of the BCG will follow the gravitational potential, such that $t_{\rm ff} \simeq r/\sigma_*$ (Voit et al. 2015). We can therefore approximate $\omega_{\rm BV}$ as $\frac{1}{t_{ff}}\sqrt{\frac{6}{5}\frac{d\ln S}{d\ln r}}$.

Our data do not allow the calculation of the entropy profile on scales $r \lesssim 25$ kpc (Figure 8), ergo we use the average slope $d\ln S/d\ln r = 0.67$ given by Hogan et al. (2017b) (see also Panagoulia et al. 2014). This returns $t_{\rm slosh} \sim 7t_{\rm ff}$. We do not know the scale of the sloshing, but it must be greater than the length of the X-ray tail (∼16 kpc). Based on the measured $\sigma_* = 226 \pm 7$ km s^{-1} (Pulido et al. 2018), at 16 kpc, $t_{\rm ff} = 70$ Myr, and therefore $t_{\rm slosh}$ may be as much as ∼490 Myr. As expected, this is considerably longer than the AGN expansion timescale, confirming that, if sloshing is occurring, it cannot yet have affected the structure of the radio lobes.

As argued by Olivares et al. (2019), the fact that filamentary nebulae in cool core clusters generally lack a significant velocity gradient indicates that the cool Hα or CO-emitting gas they contain is at least partially tied to the surrounding ICM. It is unclear how the different phases are connected, but it has been suggested that the denser material may be enveloped by many diffuse layers of warmer gas (Li et al. 2018), or threaded through by magnetic fields (McCourt et al. 2015), either of which could increase drag forces. We would thus expect the Hα emission to trace the regions in which gas has most recently cooled from the ICM, after modification by the expanding radio lobes. If the inflation of cavities has disrupted the cooling region, we might expect the locus of any future cooling to be at the new X-ray peak of surface brightness, the source of the BCG nucleus. However, the lack of Hα emission at that location suggests that cooling there is slower than it was near the BCG core, and that no reservoir of cooled material has yet built up at that location.

Of course, this scenario is speculative, given the constraints available from the data. Several aspects are uncertain. All, part, or none of the Hα emitting gas might have formed as a result of the AGN outburst, with the expanding lobes triggering condensation (e.g., Qiu et al. 2020). If the cluster is sloshing, we cannot know the scale or alignment of the motion without deeper data. However, this scenario explains several basic facts: the radio and Hα emission are correlated because the radio has at least partly determined the morphology of the Hα-emitting gas. The X-ray offset is the result of sloshing, which has not affected the radio sources or Hα because the radio source expansion timescale is short compared to the sloshing timescale. The BCG is no longer the center of ICM cooling, because the AGN has pushed aside the dense gas that fueled the outburst.

The scenario also makes testable predictions. If the cluster is sloshing, we should expect deeper Chandra data to reveal nested cold fronts, and the X-ray ridge should contain relatively cool, high-abundance gas. Deeper imaging should also allow us to more accurately measure the morphology of any cavities, which should be correlated with the radio jets and lobes. Higher-resolution radio data may be required to make this comparison. Finally, we might expect higher-resolution Hα imaging to reveal complex structure in the cooled material, consistent with a filamentary nebula disturbed by an AGN outburst.

4.5. Alternative Explanations for the Origin of the Hα Emission and Spatial Offsets

An alternative hypothesis that could explain the observed displacement of the Hα emission is cooling *in situ*, perhaps stimulated by the same AGN outburst that originated the X-ray cavities. Inhomogeneous cooling scenarios in clusters have been the object of a long, lively debate (see early reviews by

Fabian et al. (1991, 1994), and references therein). Nowadays, many lines of evidence suggest that hot gas cools at a (mean) low rate and in a spatially distributed fashion, when the ISM/ICM conditions are appropriate; see Hogan et al. (2017b), Pulido et al. (2018), and Lakhchaura et al. (2018) for a quantitative discussion. The primary trigger of this localized cooling (that is, the origin of thermally unstable perturbations) might be turbulence, e.g., chaotic cold accretion (CCA; Gaspari et al. 2012, 2013; Voit et al. 2015). It may also be attributable to lifting of low-entropy gas by X-ray cavities (Revaz et al. 2008; Brighenti et al. 2015), or to the sloshing itself.

CCA implies the triggering of thermal instabilities, which is favored by a central ($\leqslant 10$ kpc) cooling time $t_{\rm cool} \sim 1$ Gyr (Hogan et al. 2017a; Pulido et al. 2018) or by $t_{\rm cool}/t_{ff} \leqslant 10-20$ (Voit et al. 2015). It is easier for it to ensue at the position of the X-ray peak, but it can be triggered wherever these conditions are respected. Therefore, the displacement observed for the Hα gas could be the result of CCA detached from the emission peak. CCA at the current position of the peak could still be happening, but it may not yet have built up enough material to be detected in Hα. However, given the available X-ray observation, we are not in a position to accurately estimate the cooling time in the central region of the cluster.

We can explore in some more detail the scenario where the warm gas derives from a cool component of the ICM, originally located close to the nucleus of the BCG, uplifted by the cavities and then cooled to 10^4 K. Following Archimedes' principle, cavities can lift an amount of gas equal to their displacement, though simulations suggest that the maximum amount is only $\sim$50% of this value (Pope et al. 2010). This corresponds to $M_{\rm uplift} = 9 \cdot 10^6 M_\odot$ for cavity A, and $M_{\rm uplift} = 3 \cdot 10^6 M_\odot$ for cavity B. The mass of the Hα plume is lower ($M_{\rm H\alpha} \sim 2.4 \cdot 10^6 M_\odot$; see Section 4.2). However, given the state-of-the-art correlation between $L_{\rm H\alpha}$ and molecular gas mass $M_{\rm mol}$ (see, e.g., Edge 2001; Salome & Combes 2003; Pulido et al. 2018), that is usually found to be cospatial with Hα, we would expect to have $M_{\rm mol} \sim 10^9 M_\odot$ (lower than the upper limit $1.5 \times 10^9 M_\odot$ quoted by Salomé & Combes (2003)). The total amount of gas would therefore be too large for the cavities to uplift—and this, along with the radio/Hα morphology, would imply the need for an earlier cycle of AGN jet activity if uplift is responsible.

The observed Hα line emission could also be the remnant of the ISM of a gas-rich galaxy that merged with the BCG. To test this hypothesis, we examined SDSS and DSS optical images and catalogs in order to check whether a member galaxy could be interacting with the BCG. However, the closest system lies more than 40 kpc away from the BCG, not showing any hint of interplay. Therefore, the merging hypothesis looks unlikely with the current data.

Finally, the warm gas could originate from the stellar mass loss in the BCG (Mathews 1990; Li et al. 2019). With a total *B*-band luminosity $L_B \sim 1.3 \times 10^{11}\ L_{B,\odot}$ (Makarov et al. 2014) and the stellar mass to luminosity ratio of an old population $(M/L_B) \sim 7$ (e.g., Maraston 2005), the expected mass loss rate is $\dot{M}_* \sim 1.35 M_\odot/{\rm yr}$ (Mathews 1989). Thus, the observed amount of emission-line gas could be accumulated in less than 2 Myr. However, the displacement with respect to the BCG center and its filamentary and disturbed distribution (Edwards et al. 2009; Hamer et al. 2016) are not easily accounted for by this scenario.

5. Conclusions

We performed a multiwavelength analysis of the cool core cluster A1668, by means of new radio (EVLA) and X-ray (Chandra) observations and of Hα line emission data from Hamer et al. (2016). The results can be summarized as follows:

1. The radio analysis at 1.4 ($L_{1.4\ \rm GHz} \sim 6 \cdot 10^{23}$ W Hz^{-1}) and 5 GHz ($L_{5\ \rm GHz} \sim 2 \cdot 10^{23}$ W Hz^{-1}) shows a small ($\sim$11–14 kpc) and elongated FRI radio galaxy, with no hints of larger-scale emission at these frequencies. The mean spectral index is $\alpha = 0.99 \pm 0.06$, consistent with the usual values found in BCGs.
2. The X-ray analysis confirms the classification of A1668 as a cool core cluster, with a cooling radius of $\sim$40 kpc inside, for which we estimate a bolometric luminosity $L_{\rm cool} \sim 1.9 \cdot 10^{43}$ erg s^{-1}.
3. The multiwavelength analysis reveals two spatial offsets, with the first of $\sim$6 kpc being between the BCG nucleus and the X-ray peak, while the second of $\sim$7.6 kpc is between the Hα and the X-ray peaks. This is similar to what was found in another similar cluster, A2495, with two offsets of 6 and 4 kpc, respectively (Pasini et al. 2019). The compact Hα emission structure extends for $\sim$11 kpc and is mostly cospatial with the BCG, unlike A2495, where the line emission seems to be linked to the cluster cool core rather than to the central galaxy.
4. We identify three X-ray surface brightness depressions, one of them (A) coincident with the west radio lobe and with the Hα peak, another one (B) lying within the east radio lobe, and the third one (C) being more uncertain. For the system of cavities A and B, we determine an age of $\sim$5.2 Myr. The $L_{\rm cool}$–P$_{\rm cav}$ estimates for A1668 are in agreement with the relationship observed for other systems (e.g., Bîrzan et al. 2017), suggesting that the detected offsets are not able to break the AGN feeding–feedback cycle.
5. Finally, we discuss possible explanations for the multiphase gas and for the displacements observed in the core of A1668. We propose that, initially, all the components were spatially coincident in the cluster cool core. Sloshing was likely triggered by a minor merger, causing some of the cool gas around the BCG to be drawn out into a tail that we now observe as an X-ray ridge structure. On the other hand, the densest, most rapidly cooling gas, still in and around the BCG core, condensed out to form the Hα nebula. About five million years ago, the condensed material fueled the central SMBH, triggering the outburst that produced the observed radio jets/lobes. The expansion of the lobes finally pushed aside the Hα nebula and the hot ICM, disrupting the cool core center. Alternative explanations for the misplacement of the Hα emission include cooling *in situ* through thermal instabilities, uplift from the cavities, reminiscence from a past merger with a gas-rich galaxy, or stellar mass loss from the BCG, although the last three seem unlikely (see Section 4.5).

We thank the referee for thoughtful comments and suggestions, which have significantly improved the presentation of our results. T.P. is supported by the BMBF Verbundforschung under grant number 50OR1906. E.O'S. acknowledges support for this work from the National

Aeronautics and Space Administration through Chandra Award Number GO1-22125X issued by the Chandra X-ray Center, which is operated by the Smithsonian Astrophysical Observatory for and on behalf of the National Aeronautics Space Administration under contract NAS8-03060. Based on observations made with ESO Telescopes at the La Silla or Paranal Observatories under program ID 080.A-0224 and 082.B-0671. The National Radio Astronomy Observatory is a facility of the National Science Foundation, operated under cooperative agreement by Associated Universities, Inc.

ORCID iDs

T. Pasini https://orcid.org/0000-0002-9711-5554
M. Gitti https://orcid.org/0000-0002-0843-3009
F. Brighenti https://orcid.org/0000-0001-9807-8479
E. O'Sullivan https://orcid.org/0000-0002-5671-6900
F. Gastaldello https://orcid.org/0000-0002-9112-0184
P. Temi https://orcid.org/0000-0002-8341-342X
S. L. Hamer https://orcid.org/0000-0003-1932-0162

References

Anders, E., & Grevesse, N. 1989, GeCoA, 53, 197
Andreon, S. 2016, A&A, 587, A158
Arnaud, K. A. 1996, in ASP Conf. Series, 101, Astronomical Data Analysis Software and Systems V, ed. G. H. Jacoby & J. Barnes (San Francisco, CA: ASP), 17
Barbosa, C. E., Arnaboldi, M., Coccato, L., et al. 2018, A&A, 609, A78
Bayer-Kim, C. M., Crawford, C. S., Allen, S. W., Edge, A. C., & Fabian, A. C. 2002, MNRAS, 337, 938
Bîrzan, L., Rafferty, D. A., Brüggen, M., et al. 2020, MNRAS, 496, 2613
Bîrzan, L., Rafferty, D. A., Brüggen, M., & Intema, H. T. 2017, MNRAS, 471, 1766
Bîrzan, L., Rafferty, D. A., McNamara, B. R., Wise, M. W., & Nulsen, P. E. J. 2004, ApJ, 607, 800
Brighenti, F., Mathews, W. G., & Temi, P. 2015, ApJ, 802, 118
Cavagnolo, K. W., Donahue, M., Voit, G. M., & Sun, M. 2008, ApJL, 683, L107
Cavaliere, A., & Fusco-Femiano, R. 1976, A&A, 49, 137
Clarke, T. E., Blanton, E. L., & Sarazin, C. L. 2004, ApJ, 616, 178
Crawford, C. S., Allen, S. W., Ebeling, H., Edge, A. C., & Fabian, A. C. 1999, MNRAS, 306, 857
Crawford, C. S., Sanders, J. S., & Fabian, A. C. 2005, MNRAS, 361, 17
Ebeling, H., Edge, A. C., Bohringer, H., et al. 1998, MNRAS, 301, 881
Edge, A. C. 2001, MNRAS, 328, 762
Edwards, L. O. V., Robert, C., Mollá, M., & McGee, S. L. 2009, MNRAS, 396, 1953
Fabian, A. C. 2012, ARA&A, 50, 455
Fabian, A. C., Canizares, C. R., & Boehringer, H. 1994, ApJ, 425, 40
Fabian, A. C., Nulsen, P. E. J., & Canizares, C. R. 1991, A&ARv, 2, 191
Fabian, A. C., Sanders, J. S., Taylor, G. B., et al. 2006, MNRAS, 366, 417
Feretti, L., & Giovannini, G. 2008, in A Pan-Chromatic View of Clusters of Galaxies and the Large-Scale Structure, ed. M. Plionis, O. López-Cruz, & D. Hughes (Berlin: Springer), 24
Freeman, P., Doe, S., & Siemiginowska, A. 2001, Proc. SPIE, 4477, 76
Fruscione, A., McDowell, J. C., Allen, G. E., et al. 2006, Proc. SPIE, 6270, 62701V
Gaspari, M., Ruszkowski, M., & Oh, S. P. 2013, MNRAS, 432, 3401
Gaspari, M., Ruszkowski, M., & Sharma, P. 2012, ApJ, 746, 94
Gastaldello, F., Buote, D. A., Temi, P., et al. 2009, ApJ, 693, 43
Gentile, G., Rodríguez, C., Taylor, G. B., et al. 2007, ApJ, 659, 225
Ghizzardi, S., Rossetti, M., & Molendi, S. 2010, A&A, 516, A32
Giacintucci, S., Markevitch, M., Brunetti, G., et al. 2014, ApJ, 795, 73
Giacintucci, S., Markevitch, M., Cassano, R., et al. 2017, ApJ, 841, 71
Gitti, M., Brighenti, F., & McNamara, B. R. 2012, AdAst, 2012, 950641
Gitti, M., Brunetti, G., Feretti, L., & Setti, G. 2004, A&A, 417, 1
Govoni, F., Murgia, M., Markevitch, M., et al. 2009, A&A, 499, 371
Haarsma, D. B., Leisman, L., Donahue, M., et al. 2010, ApJ, 713, 1037
Hamer, S. L., Edge, A. C., Swinbank, A. M., et al. 2012, MNRAS, 421, 3409
Hamer, S. L., Edge, A. C., Swinbank, A. M., et al. 2016, MNRAS, 460, 1758
Hamer, S. L., Fabian, A. C., Russell, H. R., et al. 2019, MNRAS, 483, 4984
Hogan, M. T., Edge, A. C., Hlavacek-Larrondo, J., et al. 2015, MNRAS, 453, 1201
Hogan, M. T., McNamara, B. R., Pulido, F., et al. 2017a, ApJ, 837, 51
Hogan, M. T., McNamara, B. R., Pulido, F. A., et al. 2017b, ApJ, 851, 66
Hudson, D. S., Mittal, R., Reiprich, T. H., et al. 2010, A&A, 513, A37
Kalberla, P. M. W., Burton, W. B., Hartmann, D., et al. 2005, A&A, 440, 775
Laine, S., van der Marel, R. P., Lauer, T. R., et al. 2003, AJ, 125, 478
Lakhchaura, K., Werner, N., Sun, M., et al. 2018, MNRAS, 481, 4472
LaRoque, S. J., Bonamente, M., Carlstrom, J. E., et al. 2006, ApJ, 652, 917
Li, Y., Bryan, G. L., & Quataert, E. 2019, ApJ, 887, 41
Li, Y., Ruszkowski, M., & Tremblay, G. 2018, ApJ, 854, 91
Makarov, D., Prugniel, P., Terekhova, N., Courtois, H., & Vauglin, I. 2014, A&A, 570, A13
Maraston, C. 2005, MNRAS, 362, 799
Markevitch, M., & Vikhlinin, A. 2007, PhR, 443, 1
Mathews, W. G. 1989, AJ, 97, 42
Mathews, W. G. 1990, in Windows on Galaxies, ed. G. Fabbiano, J. S. Gallagher, & A. Renzini (Berlin: Springer), 265
McCourt, M., O'Leary, R. M., Madigan, A.-M., & Quataert, E. 2015, MNRAS, 449, 2
McDonald, M., Veilleux, S., Rupke, D. S. N., & Mushotzky, R. 2010, ApJ, 721, 1262
McNamara, B. R., & Nulsen, P. E. J. 2007, ARA&A, 45, 117
McNamara, B. R., & Nulsen, P. E. J. 2012, NJPh, 14, 055023
McNamara, B. R., Russell, H. R., Nulsen, P. E. J., et al. 2016, ApJ, 830, 79
McNamara, B. R., Wise, M., Nulsen, P. E. J., et al. 2000, ApJL, 534, L135
Mohr, J. J., Mathiesen, B., & Evrard, A. E. 1999, ApJ, 517, 627
Olivares, V., Salomé, P., Combes, F., et al. 2019, A&A, 631, A22
Panagoulia, E. K., Fabian, A. C., & Sanders, J. S. 2014, MNRAS, 438, 2341
Pasini, T., Gitti, M., Brighenti, F., et al. 2019, ApJ, 885, 111
Pope, E. C. D., Babul, A., Pavlovski, G., Bower, R. G., & Dotter, A. 2010, MNRAS, 406, 2023
Pulido, F. A., McNamara, B. R., Edge, A. C., et al. 2018, ApJ, 853, 177
Qiu, Y., Bogdanović, T., Li, Y., McDonald, M., & McNamara, B. R. 2020, NatAs, 4, 900
Rau, U., & Cornwell, T. J. 2011, A&A, 532, A71
Revaz, Y., Combes, F., & Salomé, P. 2008, A&A, 477, L33
Rossetti, M., Gastaldello, F., Ferioli, G., et al. 2016, MNRAS, 457, 4515
Salomé, P., & Combes, F. 2003, A&A, 412, 657
Sanderson, A. J. R., Edge, A. C., & Smith, G. P. 2009, MNRAS, 398, 1698
Soker, N. 2016, NewAR, 75, 1
Sutherland, R. S., & Dopita, M. A. 1993, ApJS, 88, 253
Van Dokkum, P. G., & Franx, M. 1995, AJ, 110, 2027
van Haarlem, M. P., Wise, M. W., Gunst, A. W., et al. 2013, A&A, 556, A2
Voit, G. M., Donahue, M., Bryan, G. L., & McDonald, M. 2015, Natur, 519, 203